Egypt. J. Chem. **Vol. 68**, No. 11 pp. 153 - 163 (2025)

Egyptian Journal of Chemistry

http://ejchem.journals.ekb.eg/

Synthesis of Graphene-Diamond Hybrid Using Plasma-Enhanced Chemical Vapor Deposition

Diaa Ibrahim[1*], Abdou Garamoon[2], Farouk Elakshar[2], Ashraf F.El-Sherif[3], Wafaa Soliman[4], Mansour ElSabbagh[2,5]

[1]Egyptian Academy for Engineering and Advanced Technology,Cairo,,Egypt
[2] Physics Department, Faculty of Science (male), Al-Azhar University,Cairo, Egypt
[3] Faculty of Engineering, Ahram Canadian University (ACU), Giza, Egypt
[4] Department of Laser Sciences and Interactions, National Institute of Laser Enhanced Sciences (N.I.L.E.S), Cairo University, Giza,12613,
[5]Egypt Center of Plasma Technology, Al-Azhar University,Cairo, Egypt

Abstract

A homemade Plasma-Enhanced Chemical Vapor Deposition (PECVD) system was developed to synthesize a graphene-diamond hybrid material using Radio Frequency Capacitively Coupled Plasma (RF-CCP) under high-pressure discharge conditions. This study stands out by operating RF-CCP at elevated pressures (200 and 700 mbar), an unconventional regime for this type of plasma, leading to unique dynamics in methane dissociation and reactive species formation. Optical Emission Spectroscopy (OES) identified key plasma species and predicted critical chemical pathways governing hybrid material growth. The high-energy plasma environment effectively dissociated methane, breaking its strong molecular bonds and generating reactive species such as CH and C_2, which facilitated the simultaneous deposition of sp^2-hybridized graphene and sp^3-hybridized diamond structures.

This study demonstrates the synthesis of a graphene-diamond hybrid material using RF-CCP at high pressure, Enabling precise control over its formation. Structural characterization via X-ray Diffraction (XRD), Raman spectroscopy, Fourier Transform Infrared Spectroscopy (FTIR), and Transmission Electron Microscopy (TEM) confirmed the coexistence of graphene and diamond phases. The findings suggest that CH and C_2 species played a crucial role in material formation, offering a new strategy for designing hybrid carbon materials.

Keywords: Graphene-diamond hybrid; Optical emission Spectroscopy; Plasma-Enhanced Chemical Vapor Deposition; Plasma chemistry; Raman spectroscopy.

1. Introduction

The synthesis of carbon-based materials, such as carbon nanomaterial, diamond, graphene, graphene oxide, and hybrid material has gained more attention due to their potential for a wide range of industrial and medical applications[1]. Among those materials' graphene, a single layer of carbon atoms arranged in a honeycomb lattice has garnered the most attention due to its diverse range of potential industrial applications. Its exceptional electrical and optical properties, such as atomic thickness, outstanding electrical and thermal conductivity, charge carrier mobility, superior chemical stability, high aspect ratio, and sharp edges, render it a promising material for various applications, including field electron emission and others[2,3]. In contrast, diamond boasts exceptional properties, including low compressibility, high thermal conductivity, and high strength, this makes it an ideal material for intense applications, including cutting tools, electronic devices, and magnetic disk coatings. [4]. Graphene-diamond hybrids have been attracting researcher's interest. Experiments have shown that adding diamonds to graphene converts graphene into a semiconductor with a finite band gap and stimulates the formation of electronic spin [5,6] . In addition, diamond is an ideal material to combine with graphene due to its high mechanicals' strength, efficient heat removal, and high optical phonon energy. These properties allow graphene-diamond hybrids to withstand extreme operating conditions without degrading the main characteristics of graphene, such as its linear band dispersion [7]. Graphene-diamond hybrids are promising for high-performance electronic applications in extreme conditions, particularly in the aerospace and defence industries. By hybridizing diamond with graphene, a groundbreaking approach to diamond electronics emerges. This process leverages the unique strengths of both materials, combining graphene's exceptional electronic mobility and mechanical strength with diamond's superior thermal conductivity and robustness. As a result, advanced electronic devices can be developed to operate reliably under extreme conditions. These breakthroughs highlight the need for continued research into synthesizing and applying graphene-diamond hybrid materials, paving the way for a future where these materials revolutionize the next generation of electronic technologies[8,9].

---

*Corresponding author e-mail: Diaa@eaeat.edu.eg.; (Diaa Ibrahim).

Receive Date: 22 December 2024, Revise Date: 14 March 2025, Accept Date: 18 March 2025
DOI: 10.21608/ejchem.2025.346693.11029

Graphene, diamond film, and graphene-diamond hybrid film are synthesized using thermal chemical vapor deposition (CVD)[10,11]. In CVD, a substrate (copper) induced is exposed to high temperature (~1000 °C) to enable thermal decomposition of hydrocarbon gaseous precursors such as CH_4 or C_2H_2 mixing mostly with H_2, or Ar-H_2 This process results in the deposition of the desired product on the substrate surface. However, high-temperature deposition is often impractical or undesirable for certain applications. Plasma-enhanced chemical vapor deposition (PECVD) offers an alternative approach, facilitating reaction and deposition at lower temperatures and within shorter processing time [12]. Inelastic collisions between electrons and gas molecules occur in the plasma chamber during the PECVD process, resulting in the formation of reactive species like (electrons, ions, excited atoms, etc.). Solid products are produced and deposited on the substrate surface as a result of a chemical reaction between the reactive species and the substrate. PECVD has proven effective for the low-temperature synthesis of graphene, diamond, diamond-like carbon, graphene oxide, and carbon nanotubes (CNTs). It is anticipated that graphene could emerge during the first stage of CNT formation [13]. Additionally, PECVD's ability to modify the growth rate of diamond and graphene enables the creation of hybrid structures with tailored morphologies, enhancing their applicability in specific industrial sectors, particularly those demanding materials that can perform under extreme stress or high temperatures[14]. PECVD is likely the most effective method for synthesizing high-quality, large-area graphene at a low cost, making it a highly promising technique.[15]. PECVD utilizes various plasma excitation methods, including radio-frequency (RF) discharge, direct current (DC) discharge, and microwave (MW) plasma, enabling large-area growth of graphene and diamond at relatively low substrate temperatures. [16] The PECVD process is instrumental in the simultaneous synthesis of diamonds and graphene, holding great promise for the production of high-quality hybrid materials. By enhancing the efficiency and precision of both graphene and diamond synthesis, this technique also allows for precise control over deposition conditions through the adjustment of parameters such as pressure, gas mixture, and power. Furthermore, PECVD facilitates the simultaneous growth of graphene and diamonds, enabling independent control over their formation. This level of precision is crucial for developing graphene-diamond hybrid structures with tailored properties that cater to the demands of high-performance applications. By effectively utilizing the PECVD process, it is possible to create advanced materials in a single step, effectively combining graphene's exceptional conductivity with diamond's mechanical strength and thermal stability[17].

Among the various plasma excitation methods used in PECVD, Radio Frequency Capacitively Coupled Plasma (RF-CCP) has become a cornerstone technique in thin-film deposition, particularly for carbon-based materials, due to its ability to generate stable, low-temperature plasmas. RF-CCP is widely utilized in the microelectronics industry for the preparation of functional thin films and the etching of insulated layers in semiconductor devices. The simplicity and low maintenance requirements of RF-CCP equipment make it a popular choice for these application[18,19]. However operating RF-CCP at high pressures introduces notable challenges due to variations in electron temperature and density, which directly influence plasma stability and film quality. At elevated pressures, the mean electron temperature and electron density initially decrease, followed by complex behavior influenced by the applied frequency. These dynamics significantly affect discharge characteristics, making precise control essential for maintaining consistent film deposition [20,21].

Methane (CH_4) plays a crucial role in materials science, particularly in the deposition of different carbon-based materials. Compared to other hydrocarbon gases like ethylene (C_2H_4) and acetylene (C_2H_2), methane is preferred for its ability to produce high-quality films with higher sp^3 content. This makes methane an excellent choice for applications requiring superior mechanical, optical, and electrical properties, highlighting its importance in advancing materials science [22,23]

In the current work, we present the results of fast deposition of graphene-diamond hybrid structures on a copper substrate using 13.56 MHz homemade asymmetric capacitively coupled RF discharge (as enhanced chemical vapor deposition (PECVD) system operated with an argon-methane mixture at pressures of 200 mbar, and 700 mbar while keeping the discharge power at 100 watts). Optical emission spectra of the discharge conditions were acquired and analyzed to identify the species in the discharge. The deposited material structures were characterized using X-ray diffraction (XRD), Raman spectroscopy, Transmission Electronics Microscopy (TEM), and Fourier Transform Infrared (FTIR) characterization techniques.

2. Experimental Procedure

2.1 Experimental Setup

The experimental setup is shown in Figure 1, the details of the setup are described elsewhere [24]. The most salient feature is described here. The discharge was produced between two circle-bare copper electrodes. The upper electrode was 1cm in diameter and water-cooled while the lower electrode was 6 cm in diameter. The upper electrode was connected to a 13.56 MHz RF power supply via a homemade π type matching network, which consisted of an inductor and two manually adjusted variable capacitors. The lower electrode was connected to the ground. The reflected power was minimized by adjusting the capacitances of the matching network. Both electrodes were enclosed in a stainless-steel vacuum chamber and the chamber was connected to the ground. The gap between the two electrodes was fixed at 5mm. The chamber was evacuated using a mechanical rotary pump reaching an ultimate base pressure of 2mbar. The chamber was filled with an argon-methane mixture. The discharge was ignited using RF power of 100 watts for argon-methane gas mixture pressures of 200 mbar, and 700 mbar.

2.2 Characterization Techniques

Optical emission spectroscopy (OES), of the discharge region, was monitored using a UV/visible spectrometer (model AvaSpec-Mini40) to assign the discharge species. The morphology and structure of the deposited material in the current work were examined using several characterization techniques. Transmission electron microscope (TEM) images were acquired by JEOL transmission electron microscope model JEM-2100 PLUS working with an accelerating voltage of 200k. Raman spectra were recorded using a single excitation laser wavelength of 532 nm. The Raman scattered light was collected, dispersed, and analyzed using HORIBA XploRA PLUS Raman microscope. Raman light was collected with the microscope's objective magnification of 10 and the focused spot size was 10 mm. The Raman microscope was calibrated using a crystalline silicon band at a Raman shift of 520 cm^{-1}. The crystal structure was investigated using Empyrean X-ray diffraction with Cu K_a of 1.54 Å radiation source operated at 40 kV & 30 mA. A small incident angle scan mode was used where the step size was fixed at 0.013° and scan step time of 2.5s in the scan range of $5° \leq 2\theta \leq 90°$. The deposited material was characterized by Fourier transform infrared spectroscopy (FTIR). The spectra of FTIR were acquired using Thermo Fisher Fourier transform infrared spectrophotometer model Thermo FTIR CSI 370 where the spectra were recorded in the range of 400 - 4000 cm^{-1}.

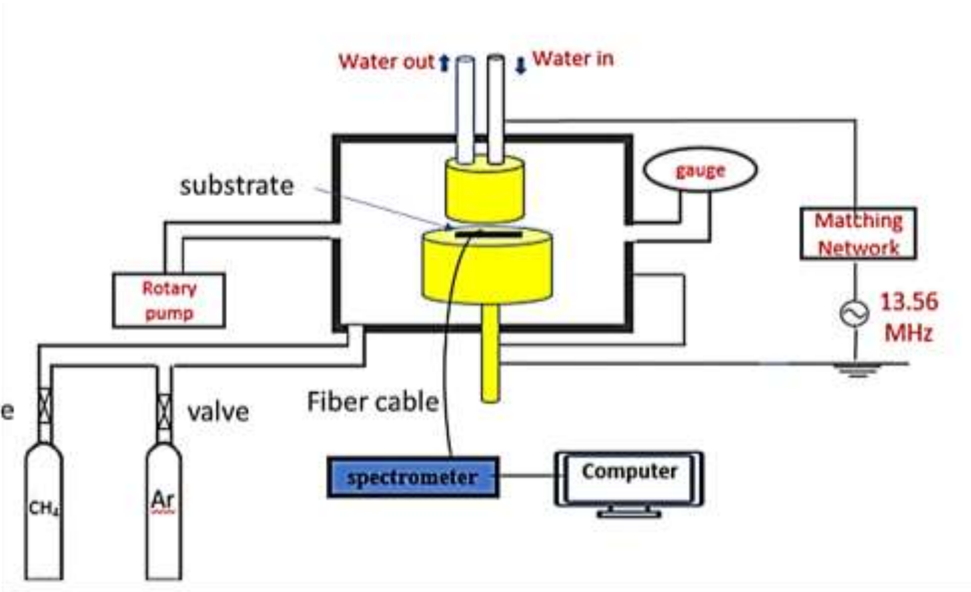

Figure 1: Experimental Setup

3. Results & Discussion

Methane (CH_4) has a unique tetrahedral molecular structure, one of the strongest bonds in all hydrocarbons, necessitating a large amount of energy to break the carbon-hydrogen bonds.[25]. The strong C-H bond in methane needs high energy to break around 434kl/mol (4.50ev). Moreover, the weak polarization of methane's C-H bonds and its symmetrical tetrahedral shape results in weak acidity (pKa = 40), making it more resistant to various reaction processes.[26]. A non-equilibrium plasma was generated in an argon-methane mixture due to the high electric field produced by the RF source. The high-electric field accelerates the electrons gaining high energy to break the C-H bond. Under the impact of high energy electrons, molecular dissociation and ionization in the system produced various radicals (O, N, H, C_2, CH_x, etc.,…)[27]. Argon plays a crucial role in methane discharge and deposition processes. It significantly enhances plasma stability, increases electron density, and facilitates the dissociation of methane. However, achieving a stable plasma using methane alone is challenging due to its high ionization energy and propensity to form complex hydrocarbons, which can lead to recombination and quenching effects.[28]. The addition of argon, which has a lower ionization energy than methane, alters critical plasma parameters such as electron density and temperature. This process enhances methane dissociation, accelerates chemical reactions, and creates a more reactive plasma environment [29]. Furthermore, argon promotes ionization processes and helps sustain stable discharge conditions, which are essential for efficient plasma-based synthesis and material processing.[30].

3.1 Optical Emission Spectroscopy

The time-averaged optical emission spectrum was collected from the center of the discharge to identify the species generated. The emission spectrum of the argon-methane discharges is depicted in Figure 2. It should be noted that the discharge was generated using 100-watt RF power and argon-methane mixture pressure of 200 mbar.

Figure 2 (a) shows the measured spectrum's UV region (350 nm – 400 nm). The emission spectra of argon-methane discharge. Figure 2 (a) reveals the presence of nitrogen second positive system (SPS: $N_2[C\ 3\Pi u] \rightarrow N_2[B\ 3\Pi g]$) emission bands, CN violet system ($B^2\Sigma^+ - X^2\Sigma^+$) emission bands, and nitrogen first negative system (FNS: $N_2^+ [B^3\Pi_g] \rightarrow N_2^+ [A^3\Sigma^+_u]$) emission bands [31]. The assigned dominant emission bands in the UV region of the measured spectra are (0,1), (1,3), & (0,2) of SPS with band heads located at 357.8, 375, and 380nm respectively, while the assigned dominant emission bands of CN violet band system are (2,2), (1,1), & (0,0) with band heads located at 385.9, 387.1and 388.3, nm respectively, and only one assigned dominant emission band of FNS, namely (0,0) band, with band head located 391.4 nm. The formation of the CN band is due to the reaction of residual N_2 in the chamber with hydrocarbon species in the plasma [32]. However, it should be noted that there are at least two different paths to producing CN bands in the discharge, both starting with interactions between active nitrogen and carbon-containing molecules. Free CN radicals form immediately from chemical interaction between these species in one of the paths. In the other path, an intermediate stable compound with a C-N bond is formed first, followed by the formation of the CN [33]. The reactions listed below represent the most likely path to produce a CN band in the discharge[34]

$$N_2 + e \rightarrow 2N^* + e \qquad (1)$$

$$N_2 + e \rightarrow 2N + e \qquad (2)$$

$$2CH_4 + N \rightarrow CH + CN + H + 3H_2 \qquad (3)$$

$$CH_x^* + N_2^* \rightarrow CN + N + H_y + H_z + e \qquad (4)$$

The measured spectra of the visible region (400 nm-700 nm) are shown in Figure 2 (b). Most of the emissions in this region are from molecular species (N_2, CN, C_2, CH, & H_2) in addition to a few weak atomic & ionic emission lines (Ar, Ar^+, & H). In this region, the strong emissions are the emission SPS with band heads located at 405 nm , and the emission of CN violet system bands (0,1), (1,2), (2,3), & (3,4) with band heads located at 416.6,420.01,423.6 and 427.7nm respectively. Moderate emissions of this region are assigned as the emission of the C_2 Swan system $(A^3\Pi_g - X'^3\Pi_u)$ bands (3,2), (2,1), (1,0), (1,1), (0,0), (2,3), (1,2), & (0,1) with band heads located at 468.1, 469.6, 471.4, 473.4, 512.5, 516.8, 553.1, 557.9, and 563.8 nm respectively. The weak emission in this region is assigned as, (0,0) band emission of CH 4300 Angstrom system $(A^2\Delta - X^2\Pi)$ which is located at 431.4 nm, The CH band formed in methane discharge due to the H abstraction of CH_x, most likely as a result of electron impact dissociation. Additionally, the CH radical can also be produced by the dissociation of methane by highly excited states of nitrogen as shown in reaction (3) [35]. Due to the rich nitrogen plasma, the intensity of the CH is very low during the experiments [36]. The notably moderate emission of C_2, in contrast to the relatively weaker emission from the CH band, suggests that the distribution of CH_x species generated from CH_4 through electron impact processes tends to favor the formation of atomic carbon species [37]. Hydrogen Balmer-alpha line H_α at 656.3 nm, and argon atomic lines located at 667.6 nm. The reactions listed below represent the most likely path to produce hydrogen, carbon, and CH band from methane [38].

$$CH_4 + e \rightarrow CH + H_2 + H + e \qquad (5)$$

$$CH_4 + e \rightarrow C + e + 2H_2 \qquad (6)$$

$$C + C \rightarrow C_2 \qquad (7)$$

It is widely recognized with methane molecules, that when electrons collide it results in the production of CH and C, as demonstrated in Equations (5 and 6) with dissociation energies of 12.5 and 14 eV, respectively [39].

The formation of graphene-diamond hybrid films is significantly influenced by the crucial roles of C_2 and CH species. Specifically, C_2 species facilitate the growth of graphene by enabling the formation of sp^2 hybridized carbon networks, a structural necessity for graphene. In contrast, CH radicals exhibit a dual functionality, not only contributing to the formation of diamond through sp^3 hybridization but also supporting the growth of graphene. The delicate balance between these species within the plasma environment gives rise to the simultaneous deposition of both materials. Here, C_2 species predominantly favor graphene growth, while CH species exert an influence on the development of both graphene and diamond, ultimately yielding a hybrid structure characterized by its unique properties[40]

Figure 3 (c) shows the measured spectra in the near-infrared region. The emissions in this region are assigned as argon atomic lines with only one very weak oxygen atomic line located at 777.2 nm.

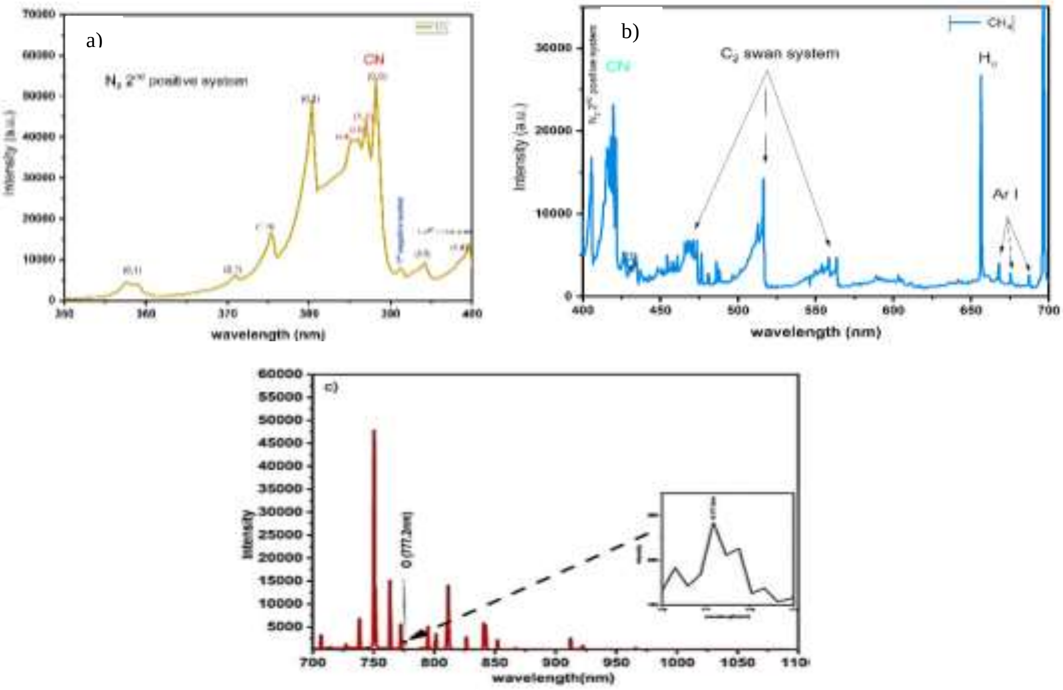

Figure 2:The emission spectra of argon-methane discharg a) UV region b) Vis region c) IR region

3-2 Structural Characterization

During the discharge of argon-methane mixtures, a black material was deposited from the gas phase. This black material was deposited on commercial copper substrates with a thickness of 25 μm and impurities listed in Table 1. The impurities are detected by elemental analysis XRF before cleaning substrates with ethanol or using sonication. The most abundant impurity is silicon, which might be attributed to the sandpaper that adjusts the surface's roughness

Table 1:Impurities of copper substrate

Elements	Weight (%)
Cu	99.8
Al	0.015
Si	0.11
Pb	0.040
Zn	0.0032
Ni	0.0178
Fe	0.014

3.2.1 TEM:

Figure 3 shows TEM images captured at different locations to represent the morphology of the material deposited during the discharge operated at argon-methane pressures of 200 mbar, and 700 mbar. The images in Figure 6 showed deposited hybrid structures where nanoparticles (cubic diamond & hexagonal diamond phases as confirmed from XRD and Raman spectroscopic data) were deposited over flat and crumpled transparent sheets and nanotubes. The wrinkled structure of the flake is notably like thin films made using graphene sheets, consistent with earlier observations[41]. Regarding the discharge of argon-methane pressures of 200 mbar and 700 mbar cases, some images in Figure 3 showed that some nanotubes were rolled up in shredded sheets. TEM images of Figure 3 showed deposition of wrinkled and folded long sheets with a few tens of mm in length. The sheets in the TEM images could be graphene, or graphene oxide, or copper sheets or a combination of them., since the material used during the deposition is hydrocarbon and copper substrate.

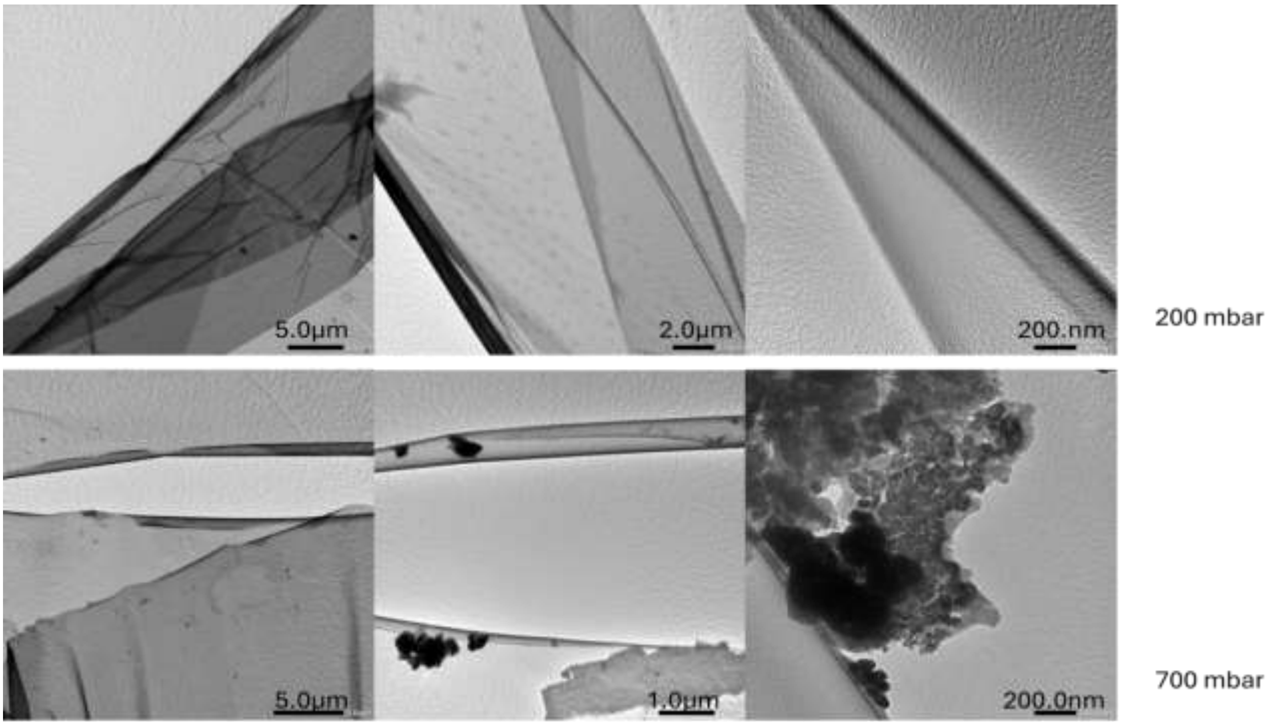

Figure 3: TEM images of deposited material obtained from the discharge of argon-methane mixture operated at pressures of 200 mbar & 700 mbar.

3.2.2 FTIR:

Figure 4 shows FTIR spectra of deposited material obtained from the discharge of argon-methane mixture operated at pressures of 200 mbar & 700 mbar. The assignments of the FTIR spectra shown in Figure 4 was performed, based on literature and the free online database 'INSTA NANO FTIR "[42]. The assignments represent possible functional groups and compounds of the material deposited in argon-methane discharge operated at 200 mbar and 700 mbar pressures. The O-H band at 3434.5 cm^{-1} is notably narrow, and the absence of the carbonyl group (C=O) at 1717 cm-1 provides strong evidence that the deposited film is not graphene oxide[43,44]. The peak at 2924 .7 and 2857.4 cm^{-1} showed sp^3 C-H stretching vibrations bonding. The dips in FTIR spectra in the 2950-2857 cm^{-1} range are due to symmetric and asymmetric vibration frequencies of sp^3 and sp^2 stretching modes. The peak at 1627 cm^{-1} is assigned to the C=C bond stretching. The presence of C=C bonds indicates that the films contain multilayer graphene sheets, environmental CO_2 was observed around 2349 cm^{-1}.[45].

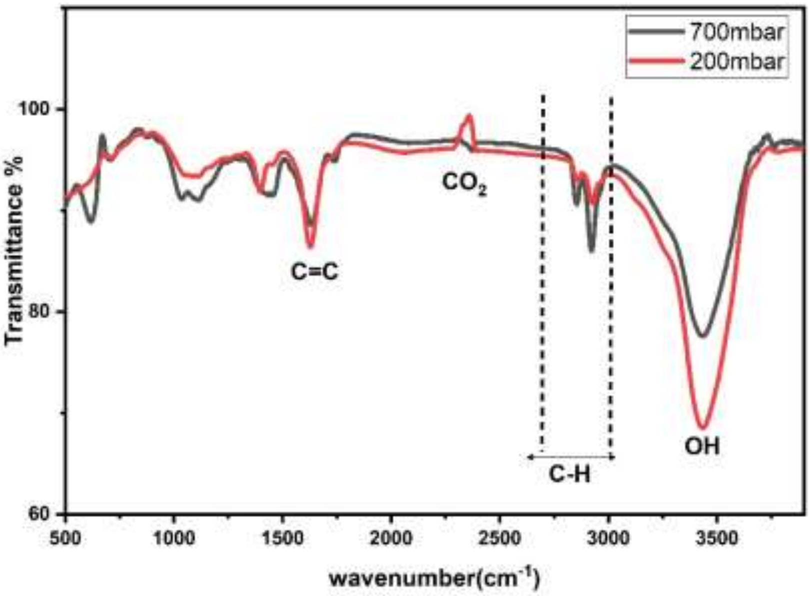

Figure 4 : FTIR spectra of deposited material obtained from the discharge of argon-methane mixture operated at pressures of 200 mbar & 700 mbar.

3.2.3 Raman Spectroscopy:

Raman spectroscopy is a powerful characterization technique to study the structure of different carbon allotropes. These spectra represent the structures of the deposited material since the laser beam is focused on the surface to avoid any contribution of the substrate material. The D, G, and 2D bands are the most prominent in the Raman spectra of graphitic carbon-based materials. The Raman bands 1200-1450, 1500-1600, and 2600-2900 cm^{-1} are the D, G, and 2D bands respectively. The G band highlights the optical E_{2g} phonons at the Brillouin zone center induced by sp^2 carbon bond stretching. The D band represents the aromatic ring breathing mode caused by the sample defect. The 2D band is attributed to double resonance transitions, which result in the creation of two phonons with opposite momentum, and this band is proportional to the number of graphene layers. The 2D band is a Raman scattering peak of particular interest because it can be used to determine the number of graphene layers in a material. In single-layer graphene, the 2D band is a single, narrow peak that a Lorentzian function can fit. Bilayer graphene has a much broader and up-shifted 2D band than single-layer graphene due to its special electronic structure, which consists of two conduction bands and two valence bands. However, for multi-layer samples, the 2D feature becomes significantly broader and asymmetric.[46]

Figure 5 shows measured Raman spectra of deposited material at argon-methane mixture pressures of 200 mbar, and 700 mbar. The deconvolutions of the measured Raman spectra are performed using Lorentz fitting, also shown in Figure 5. The deconvolution reveals many underlying peaks with incomparable widths corresponding to D, G, and 2D bands.

The deconvolution of the measured Raman spectrum of the discharge condition operated at an argon-methane pressure of 200 mbar as shown in Figure 5a, showed many peaks Raman peaks observed at 1064.7,1120 and 1443cm^{-1} are attributed to carbon-carbon (C–C) stretching and CH_2 and CH_3 deformation respectively[47]. The peak at 1331.2 cm^{-1} is attributed to the formation of cubic diamond [48], D and G bands that appeared at 1372, and 1562 cm^{-1} respectively are attributed to the disorder induced in sp^2 in carbon bond. In the 2500 - 3000 cm^{-1} range, multiple fittings were observed within the 2D region, with peaks appearing at 2672 cm^{-1}, suggesting the presence of multi-layered graphene in the material.

The deconvolution of the measured Raman spectrum of the material deposited during the discharge of argon-methane mixture at a pressure of 700 mbar as shown in Figure 5b, showed a Raman peak at 1331 cm^{-1} which is attributed to the formation of the cubic diamond. Raman peaks that appeared at 1361, 1566, and 2793 cm^{-1} are identified as D, G, and 2D bands respectively of graphene sheets [49]. Additionally, 2D band is broader and the ratio of I_{2D}/I_G is less than 1 for all the discharge conditions which confirms the deposition of a few layers of graphene [50].The Raman data supports the finding of TEM images of the deposition of hybrid sheets with nanoparticles namely graphene-diamond hybrid, where a cubic and hexagonal diamonds are deposited over a few layers of graphene sheets. The Raman data also supports the FTIR findings of the absence of graphene oxide in the deposited material which indicated the deposition of graphene.

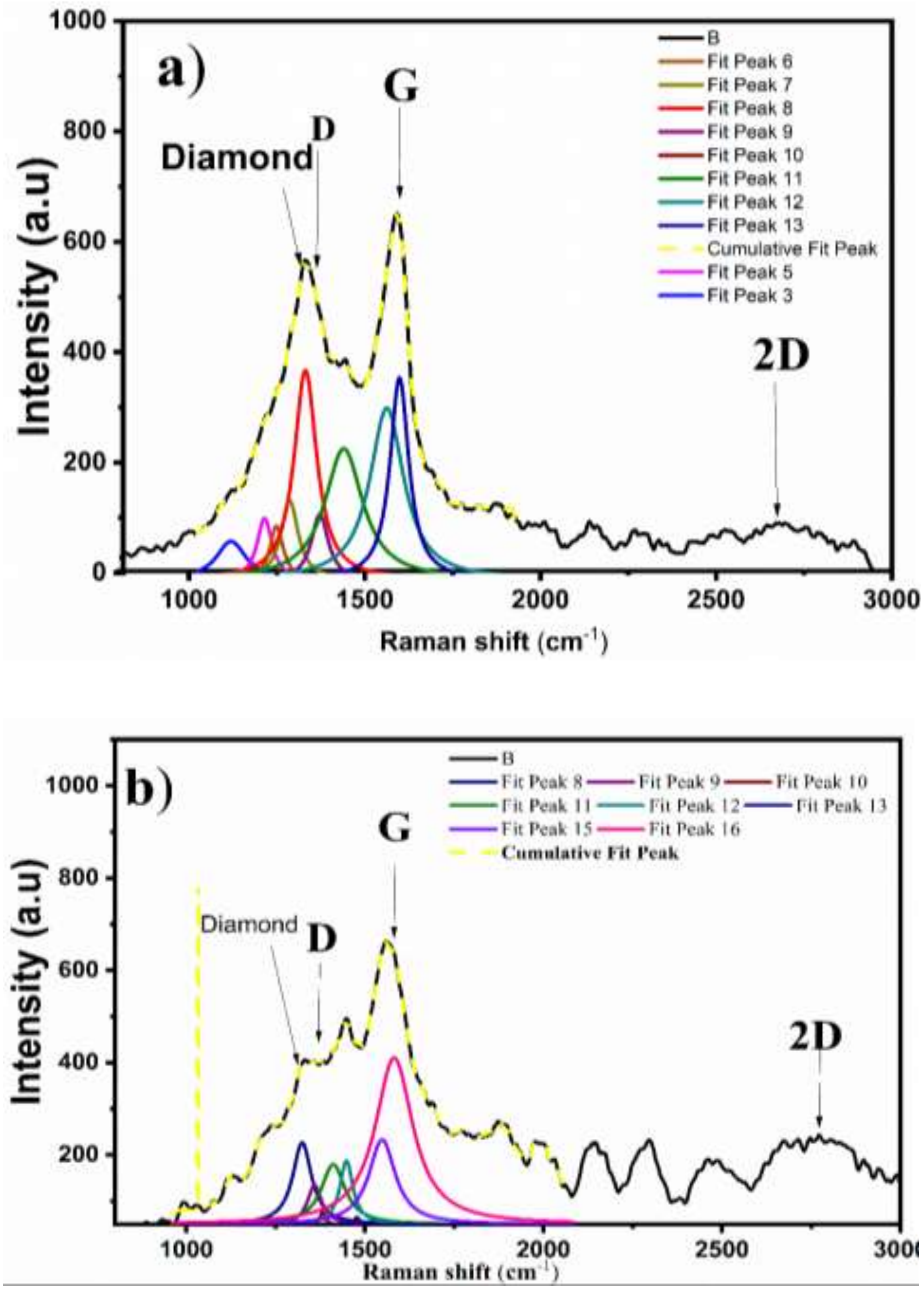

Figure 5 : Raman spectra of deposited material obtained from the discharge of argon-methane mixture operated at pressures a) 200 mbar & b)700 mbar.

3.2.4 XRD:

X-ray diffraction (XRD) is a valuable technique for characterizing the crystalline properties of materials. By utilizing XRD, we can thoroughly analyze the characteristics of deposited materials. The peaks in an XRD pattern play a crucial role in identifying the phases and properties of particles. Notably, the width of these peaks serves as an indicator of the average crystalline size of nanoparticles. Specifically, sharp peaks indicate a larger crystalline size, whereas broader peaks suggest a smaller crystal size. This distinction is significant for understanding the material's structure and potential applications[51]. Samples of the deposited material on the copper substrate were carefully placed in the XRD device, ensuring no scraping or alteration occurred. The XRD patterns of the deposited material during the discharge of an argon-methane mixture at pressures of 200 mbar, and 700 mbar are depicted in Figure 6. The key data, including the 2θ values, the identified compounds, and the card number are listed in Table 2, based on the elemental analysis of the copper substrate and possible carbon allotropes and compounds that could form within the discharge. Notably, broad peaks in Figure 6 suggest that the deposited material is a nanomaterial. The card numbers associated with each material are in agreement with the Crystallographic Open Database(COD) Card Numbers [52].

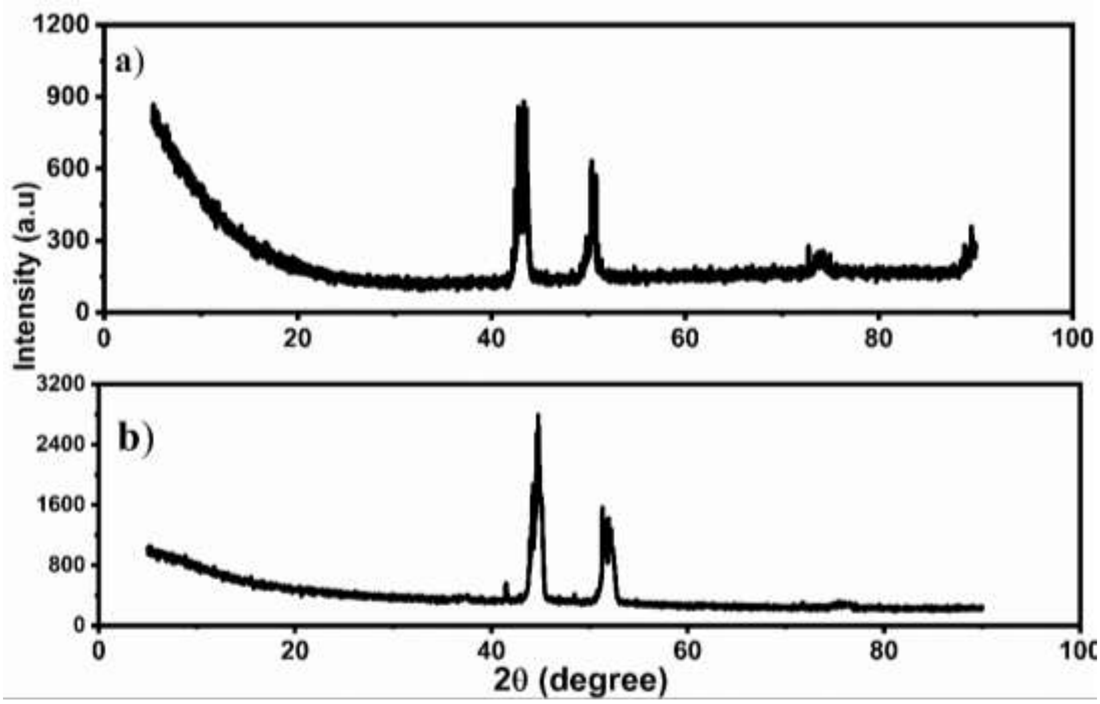

Figure 6: XRD of the deposited materials obtained from the discharge of argon-methane mixture operated at pressures of a) 200 mbar & b) 700 mbar.

Table 2: The 2θ position for diamond and copper deposits at different pressures

Pressure	2θ	Deposited material	Card number
200 mbar	42.7,43.9,	Hexagonal diamond	96-901-2591
	42.6,49.6,72.7	Copper	96-901-3021
700 mbar	43.9,75.2	Cubic diamond	96-901-2290

Graphene-related XRD peaks were not seen in Figures 6 while it was confirmed by TEM images and Raman spectra shown in Figures 3 and 5 respectively. The absence of graphene-related peaks of XRD patterns shown in Figure 6 can be ascribed to one of the following two reasons:

i: The low diffraction intensity and graphene concentration [53].
ii: Because of graphene is a two-dimensional material that does not exhibit X-ray diffraction[54].

Conclusion

In this study, for the first time (to our knowledge), a graphene-diamond hybrid material was successfully deposited on a copper substrate at relatively low temperatures using a homemade (PECVD) system with an asymmetric capacitively coupled RF discharge. The process was conducted over a wide range of argon-methane mixture pressures (200 mbar to 700 mbar) while maintaining a constant RF discharge power of 100 watts. Optical emission spectroscopy (OES) revealed that methane molecules were primarily decomposed via electron impact, producing carbon, hydrogen, and CH radicals, which were critical to the hybrid material's formation.

TEM images confirmed that the deposited material exhibited a hybrid structure comprising graphene sheets and diamond. These findings were supported by Raman spectroscopy, which verified the formation of a few-layer graphene-diamond hybrid. XRD analysis further confirmed the presence of cubic and hexagonal diamond phases within the material. Additionally, FTIR identified functional groups such as, O-H, and C=C, while the absence of carbonyl groups ruled out the presence of graphene oxide in the deposited material. This study provides new insights into the low-temperature synthesis of graphene-diamond hybrid materials using PECVD, emphasizing the critical role of plasma chemistry and reactive species in determining the material's structural properties.

Conflict of Interest

the authors declare that they have no Conflict of interest regarding the publication of this article

Acknowledgments

Coaxial Power Systems Ltd, England, is highly acknowledged for repairing the used RF power supply. This work was supported by the Science, Technology, & Innovation Funding Authority (STDF), project number CB 22896.

References

[1] Z. Liu *et al.*, "Synthesis of carbon-based nanomaterials and their application in pollution management," *Nanoscale Adv.*, vol. 4, no. 5, pp. 1246–1262, 2022, doi: 10.1039/d1na00843a.

[2] S. H. B. Vinoth Kumar, R. Muydinov, and B. Szyszka, "Plasma assisted reduction of graphene oxide films," *Nanomaterials*, vol. 11, no. 2, pp. 1–37, 2021, doi: 10.3390/nano11020382.

[3] K. J. Sankaran *et al.*, "Enhancement of plasma illumination characteristics of few-layer graphene-diamond nanorods hybrid," *Nanotechnology*, vol. 28, no. 6, 2017, doi: 10.1088/1361-6528/aa5378.

[4] D. Varshney *et al.*, "Electron Emission of Graphene-Diamond Hybrid Films Using Paraffin Wax as Diamond Seeding Source," *World J. Nano Sci. Eng.*, vol. 02, no. 03, pp. 126–133, 2012, doi: 10.4236/wjnse.2012.23016.

[5] K. S. Novoselov *et al.*, "Electric field in atomically thin carbon films," *Science (80-.).*, vol. 306, no. 5696, pp. 666–669, 2004, doi: 10.1126/science.1102896.

[6] Y. Ma, Y. Dai, M. Guo, and B. Huang, "Graphene-diamond interface: Gap opening and electronic spin injection," *Phys. Rev. B - Condens. Matter Mater. Phys.*, vol. 85, no. 23, p. 235448, 2012, doi: 10.1103/PhysRevB.85.235448.

[7] J. Yu, G. Liu, A. V. Sumant, V. Goyal, and A. A. Balandin, "Graphene-on-diamond devices with increased current-carrying capacity: Carbon sp 2-on-sp 3 technology," *Nano Lett.*, vol. 12, no. 3, pp. 1603–1608, 2012, doi: 10.1021/nl204545q.

[8] A. F. Carvalho *et al.*, "Simultaneous CVD synthesis of graphene-diamond hybrid films," *Carbon N. Y.*, vol. 98, pp. 99–105, 2016, doi: 10.1016/j.carbon.2015.10.095.

[9] K. P. S. S. Hembram, S. Lee, H. Im, H. Ju, S. H. Jeong, and J. K. Lee, "The surface hybridization of diamond with vertical graphene: A new route to diamond electronics," *Mater. Horizons*, vol. 7, no. 2, pp. 470–476, 2020, doi: 10.1039/c9mh01588d.

[10] N. F. Santos, U. Zubets, A. F. Carvalho, A. J. S. Fernandes, L. Pereira, and F. M. Costa, "Tuning the field emission of graphene-diamond hybrids by pulsed methane flow CVD," *Carbon N. Y.*, vol. 122, pp. 726–736, 2017, doi: 10.1016/j.carbon.2017.07.024.

[11] C. M. Seah, S. P. Chai, and A. R. Mohamed, "Mechanisms of graphene growth by chemical vapour deposition on transition metals," *Carbon N. Y.*, vol. 70, pp. 1–21, 2014, doi: 10.1016/j.carbon.2013.12.073.

[12] A. Adetayo and D. Runsewe, "Synthesis and Fabrication of Graphene and Graphene Oxide: A Review," *Open J. Compos. Mater.*, vol. 09, no. 02, pp. 207–229, 2019, doi: 10.4236/ojcm.2019.92012.

[13] A. Jafari, M. Ghoranneviss, M. R. Hantehzadeh, and A. Boochani, "Effect of plasma power on growth of multilayer graphene on copper using plasma enhanced chemical vapour deposition," *J. Chem. Res.*, vol. 40, no. 1, pp. 40–43, 2016, doi: 10.3184/174751916X14497648744542.

[14] G. Zhang *et al.*, "Orientated growth the 3D diamond/graphene hybrid arrays and the application in thermal interface materials," *Funct. Diam.*, vol. 2, no. 1, pp. 263–270, 2022, doi: 10.1080/26941112.2023.2169080.

[15] J. Kim, M. Ishihara, Y. Koga, K. Tsugawa, M. Hasegawa, and S. Iijima, "Low-temperature synthesis of large-area graphene-based transparent conductive films using surface wave plasma chemical vapor deposition," *Appl. Phys. Lett.*, vol. 98, no. 9, pp. 2011–2014, 2011, doi: 10.1063/1.3561747.

[16] Y. Liu, J. He, N. Zhang, W. Zhang, Y. Zhou, and K. Huang, "Advances of microwave plasma-enhanced chemical vapor deposition in fabrication of carbon nanotubes: a review," *J. Mater. Sci.*, vol. 56, no. 22, pp. 12559–12583, 2021, doi: 10.1007/s10853-021-06128-1.

[17] M. A. Lieberman and A. J. Lichtenberg, *Principles of Plasma Discharges and Materials Processing: Second Edition*, 2nd ed. Hoboken, New Jersey: John Wiley & Sons, Inc, 2005. doi: 10.1002/0471724254.

[18] Y. Ohtsu, “Physics of High-Density Radio Frequency Capacitively Coupled Plasma with Various Electrodes and Its Applications,” in *Plasma Science and Technology - Basic Fundamentals and Modern Applications*, IntechOpen, 2019. doi: 10.5772/intechopen.78387.

[19] Y. Ohtsu, “High-density radio-frequency plasma sources produced by capacitive discharge with various methods for thin-film preparation,” *IEEJ Trans. Fundam. Mater.*, vol. 130, no. 10, pp. 865–870, 2010, doi: 10.1541/ieejfms.130.865.

[20] G. Q. Yin, J. J. Wang, and Q. H. Yuan, “The Discharge Characteristics of Capacitively Coupled Ar Plasma as the Change of Pressure,” *Plasma Phys. Reports*, vol. 49, no. 6, pp. 802–807, 2023, doi: 10.1134/S1063780X23600135.

[21] H. J. Kim, “Influence of the gas pressure in a Torr regime capacitively coupled plasma deposition reactor,” *Plasma Sources Sci. Technol.*, vol. 30, no. 6, p. 65001, 2021, doi: 10.1088/1361-6595/abef17.

[22] D. F. Franceschini, F. L. Freire, and S. R. P. Silva, “Influence of precursor gases on the structure of plasma deposited amorphous hydrogenated carbon-nitrogen films,” *Appl. Phys. Lett.*, vol. 68, no. 19, p. 2645, 1995, doi: 10.1063/1.116268.

[23] S. Hofmann, B. Kleinsorge, C. Ducati, A. C. Ferrari, and J. Robertson, “Low-temperature plasma enhanced chemical vapour deposition of carbon nanotubes,” *Diam. Relat. Mater.*, vol. 13, no. 4–8, pp. 1171–1176, 2004, doi: 10.1016/j.diamond.2003.11.046.

[24] D. Ibrahim, A. Garamoon, F. Elakshar, and A. Alsharif, “Electrical and Optical Characteristics of Wide Pressure-Range Capacitive Coupled RF Discharge,” *Al-Azhar Bull. Sci.*, vol. 34, no. 2, p. 10, 2023, doi: 10.58675/2636-3305.1645.

[25] C. Bai, S. Li, T. Chen, X. Chen, W. Meng, and J. Pan, “Methane-Air Plasma-Assisted Ignition Excited by Nanosecond Repetitively Pulsed Discharge: Numerical Modeling and Effect of Inert Gas,” *ACS Omega*, vol. 6, no. 37, pp. 24156–24165, 2021, doi: 10.1021/acsomega.1c03696.

[26] J. Feng *et al.*, “Plasma-Assisted Reforming of Methane,” *Adv. Sci.*, vol. 2203221, pp. 1–36, 2022, doi: 10.1002/advs.202203221.

[27] L. Tang, X. Yang, K. Zhao, and H. Huang, “Experimental study on high frequency capacitively coupled plasma–catalysis hybrid system for methane complete oxidation,” *Atmos. Pollut. Res.*, vol. 10, no. 1, pp. 24–29, 2019, doi: 10.1016/j.apr.2018.04.007.

[28] J. Feng *et al.*, “Plasma-Assisted Reforming of Methane,” *Adv. Sci.*, vol. 9, no. 34, p. 2203221, 2022, doi: 10.1002/advs.202203221.

[29] B. Kakati, S. S. Kausik, M. Bandyopadhyay, B. K. Saikia, and Y. C. Saxena, “Effect of argon addition on plasma parameters and dust charging in hydrogen plasma,” *J. Appl. Phys.*, vol. 116, no. 16, 2014, doi: 10.1063/1.4898858.

[30] A. Saifutdinov and B. Timerkaev, “Simulation of Arc Discharge in an Argon/Methane Mixture, Taking into Account the Evaporation of Anode Material in Problems Related to the Synthesis of Functional Nanostructures,” *Nanomaterials*, vol. 15, no. 1, p. 54, 2025, doi: 10.3390/nano15010054.

[31] A. Abdelradi, A. Samir, F. Elakshar, A. Garamoon, and M. ElSabbagh, “Characterization of atmospheric-pressure DC-glow discharge in contact with liquid with a miniature argon flow,” *Egypt. J. Chem.*, vol. 65, no. 1, pp. 99–106, 2022, doi: 10.21608/EJCHEM.2021.86067.4173.

[32] G. Alcouffe *et al.*, “Capacitively coupled plasma used to simulate Titan’s atmospheric chemistry,” *Plasma Sources Sci. Technol.*, vol. 19, no. 1, 2010, doi: 10.1088/0963-0252/19/1/015008.

[33] S. F. Durrant, N. Marçal, S. G. Castro, R. C. G. Vinhas, M. A. B. De Moraes, and J. H. Nicola, “Mechanisms of polymer film deposition from r.f. discharges of acetylene, nitrogen and helium mixtures,” *Thin Solid Films*, vol. 259, no. 2, pp. 139–145, 1995, doi: 10.1016/0040-6090(94)06439-3.

[34] A. P. L. Je´re´my Pereira, Ve´ronique Massereau-Guilbaud, Isabelle Ge´raud-Grenier, “CH and CN Radical Contribution in the Particle Formation Generated in a Radio-Frequency,” *Plasma Process. Polym*, pp. 633–640, 2005, doi: 10.1002/ppap.200500014.

[35] A. Yanguas-Gil, K. Focke, J. Benedikt, and A. Von Keudell, “Optical and electrical characterization of an atmospheric pressure microplasma jet for ArC H4 and Ar C2 H2 mixtures,” *J. Appl. Phys.*, vol. 101, no. 10, 2007, doi: 10.1063/1.2714646.

[36] V. Massereau-Guilbaud, J. Pereira, I. Ǵraud-Grenier, and A. Plain, “Influence of the power on the particles generated in a low pressure radio frequency nitrogen-rich methane discharge,” *J. Appl. Phys.*, vol. 105, no. 3, 2009, doi: 10.1063/1.3072664.

[37] N. N. Morgan and M. ElSabbagh, “Hydrogen Production from Methane Through Pulsed DC Plasma,” *Plasma Chem. Plasma Process.*, vol. 37, no. 5, pp. 1375–1392, 2017, doi: 10.1007/s11090-017-9829-3.

[38] S. Heijkers, M. Aghaei, and A. Bogaerts, “Plasma-Based CH4 Conversion into Higher Hydrocarbons and H2: Modeling to Reveal the Reaction Mechanisms of Different Plasma Sources,” *J. Phys. Chem. C*, vol. 124, no. 13, pp. 7016–7030, 2020, doi: 10.1021/acs.jpcc.0c00082.

[39] R. K. Janev and D. Reiter, “Collision processes of CHy and CHy+ hydrocarbons with plasma electrons and protons,” *Phys. Plasmas*, vol. 9, no. 9, p. 4071, 2002, doi: 10.1063/1.1500735.

[40] S. Gottlieb, N. Wöhrl, S. Schulz, and V. Buck, “Simultaneous synthesis of nanodiamonds and graphene via plasma enhanced chemical vapor deposition (MW PE-CVD) on copper,” *Springerplus*, vol. 5, no. 1, 2016, doi: 10.1186/s40064-016-2201-x.

[41] P. Pham, “A Library of Doped-Graphene Images via Transmission Electron Microscopy,” *C*, vol. 4, no. 2, p. 34, 2018, doi: 10.3390/c4020034.

[42] “INSTA NANO FTIR.” [Online]. Available: https://instanano.com/all/characterization/ftir/ftir-functional-group-

search
[43] Z. Çiplak, N. Yildiz, and A. Cąlimli, "Investigation of graphene/Ag nanocomposites synthesis parameters for two different synthesis methods," *Fullerenes Nanotub. Carbon Nanostructures*, vol. 23, no. 4, pp. 361–370, 2015, doi: 10.1080/1536383X.2014.894025.
[44] M. Aziz, F. S. A. Halim, and J. Jaafar, "Preparation and characterization of graphene membrane electrode assembly," *J. Teknol. (Sciences Eng.*, vol. 69, no. 9, pp. 11–14, 2014, doi: 10.11113/jt.v69.3388.
[45] G. Liu, X. Wei, L. Qiang, B. Zhang, and K. Gao, "Electrochemical Deposition of DLC Films Embedded with Crystalline Graphite and Multilayer Graphene," *J. Electron. Mater.*, vol. 50, no. 3, pp. 1552–1557, 2021, doi: 10.1007/s11664-020-08703-9.
[46] L. M. Malard, M. A. Pimenta, G. Dresselhaus, and M. S. Dresselhaus, "Raman spectroscopy in graphene," *Phys. Rep.*, vol. 473, no. 5–6, pp. 51–87, 2009, doi: 10.1016/j.physrep.2009.02.003.
[47] D. Varshney, C. Venkateswara Rao, M. J. F. Guinel, Y. Ishikawa, B. R. Weiner, and G. Morell, "Free standing graphene-diamond hybrid films and their electron emission properties," *J. Appl. Phys.*, vol. 110, no. 4, 2011, doi: 10.1063/1.3627370.
[48] R. Haubner and M. Rudigier, "Raman characterisation of diamond coatings using different laser wavelengths," *Phys. Procedia*, vol. 46, pp. 71–78, 2013, doi: 10.1016/j.phpro.2013.07.047.
[49] H. Kato, N. Itagaki, and H. J. Im, "Growth and Raman spectroscopy of thickness-controlled rotationally faulted multilayer graphene," *Carbon N. Y.*, vol. 141, pp. 76–82, 2019, doi: 10.1016/j.carbon.2018.09.017.
[50] D. C. Smith and G. Godard, "UV and VIS Raman spectra of natural lonsdaleites: Towards a recognised standard," *Spectrochim. Acta - Part A Mol. Biomol. Spectrosc.*, vol. 73, no. 3, pp. 428–435, 2009, doi: 10.1016/j.saa.2008.10.025.
[51] V. A. Davydov *et al.*, "Size-dependent phase transition of diamond to graphite at high pressures," *J. Phys. Chem. C*, vol. 111, no. 35, pp. 12918–12925, 2007, doi: 10.1021/jp073576k.
[52] "Crystallographic open database." [Online]. Available: https://www.crystallography.net/cod/7033336.html
[53] H. Liu *et al.*, "Incorporation of reduced graphene oxide into faceted flower-like f001g TiO2 for enhanced photocatalytic activity," *R. Soc. Open Sci.*, vol. 5, no. 8, 2018, doi: 10.1098/rsos.180613.
[54] E. Solati, E. Vaghri, and D. Dorranian, "Effects of wavelength and fluence on the graphene nanosheets produced by pulsed laser ablation," *Appl. Phys. A Mater. Sci. Process.*, vol. 124, no. 11, pp. 1–9, 2018, doi: 10.1007/s00339-018-2176-2.

.